

Biased Cell Migration of Fibroblasts Exhibiting Contact Guidance in Oriented Collagen Gels

RICHARD B. DICKINSON,* STEFANO GUIDO,† and ROBERT T. TRANQUILLO

Department of Chemical Engineering and Materials Science, University of Minnesota, Minneapolis, MN

Abstract—We present here the first quantitative correlation for cell contact guidance in an oriented fibrillar network in terms of biased cell migration. The correlation is between the anisotropic cell diffusion parameter, $D_A = D_x/D_y$, and the collagen gel birefringence, Δn , a measure of axially biased collagen fibril orientation in the x -direction. The cell diffusion coefficients, D_x and D_y , measure the dispersal of cells in the directions coincident with and normal to the axis of fibril orientation, respectively. Three essential methodological components are involved: (i) exploiting the orienting effect of a magnetic field on collagen fibrils during fibrillogenesis to systematically prepare uniform axially oriented collagen gels; (ii) using a microscope/image analysis workstation with precise, computer-controlled rotating and translating stages to automate birefringence measurement and, along with rapid “coarse optical sectioning” via digital image processing, to enable 3-D cell tracking of many cells in multiple samples simultaneously; and (iii) employing a rigorous statistical analysis of the cell tracks to estimate the magnitude and precision of the direction-dependent cell diffusion coefficients, D_x and D_y , that define D_A . We find that this measure of biased migration in contact guidance (D_A) increases with increasing collagen fibril orientation (Δn) due mainly to a rapid enhancement of migration along the axis of fibril orientation at low levels of fibril orientation, and to a continued suppression of migration normal to the axis of fibril orientation at high levels of fibril orientation.

Keywords—Contact guidance, Collagen gel, Migration, Fibroblasts, Image analysis.

Acknowledgments—This research has been supported by a National Science Foundation Presidential Young Investigator Award (BCS-8957736) and matching funds from The Procter & Gamble Company to RTT. Valuable technical assistance by Alina Ruta and Bruce Bromberek, technical advice by Jeff Shearer and Vance Fiegal, the generous provision of laboratory facilities by Drs. David Knighton and Michael Caldwell (Department of Surgery), and the usage of the magnets in the Center for Magnetic Resonance Research and the laboratory of Prof. Bruce Hammer (Department of Radiology) are all gratefully acknowledged.

*Current address: Department of Chemical Engineering, University of Florida, Gainesville, FL 32611-2022.

†Current address: Università Degli Studi di Napoli Federico II, Dipartimento di Ingegneria Chimica, P. le V. Tecchio, 80121 Napoli, Italy.

Address correspondence to Robert T. Tranquillo, Department of Chemical Engineering and Materials Science, University of Minnesota, Minneapolis, MN 55455.

(Received 2Feb94, Accepted 24Mar 94)

INTRODUCTION

The movement of a cell exhibiting contact guidance is characterized as bidirectional, a cell having maximum probabilities of migrating in two opposite directions (7). The basis for a complete methodology to quantify systematically the correlation between biased cell migration and collagen fibril orientation for cells cultured in an oriented collagen gel, a model system for cell contact guidance in a tissue having oriented ECM fibers, has recently been proposed (12). The elements of our methodology include: (i) exploiting the orienting effect of a magnetic field on collagen fibrils during fibrillogenesis to systematically and reproducibly prepare axially oriented collagen gels; (ii) measuring the gel birefringence to characterize the fibril orientation; (iii) measuring the biased cell migration to characterize the contact guidance response; and (iv) developing an empirical correlation between gel birefringence and fibril orientation. In that paper, we presented methods and results for (i) to (iii), including the automation of (ii) and (iii) via computer-controlled staging and image analysis, but for (iii), we presented a contact guidance correlation for fibroblasts in terms of biased cell orientation measured from static images. Although that is the first reported correlation for cell contact guidance in any three-dimensional (3-D) tissue-equivalent environment, it does not address the other, arguably more important, aspect of the contact guidance response, namely, biased cell migration. Here, we present our methods and results for fibroblast contact guidance in terms of biased migration obtained from 3-D cell tracking and rigorous statistical analysis of the cell tracks.

We first review three published studies directly relevant to ours: the study of contact guidance of human polymorphonuclear leukocytes (PMN), characterized by cell orientation and biased migration, on various structurally anisotropic planar substrata (anisotropic 2-D substrata) by Matthes and Gruler (18) and the studies of random migration of human fibroblasts by Noble and coworkers (21,22) and human PMN by Parkhurst and Saltzman (24) in isotropic collagen gels (isotropic 3-D substratum). There is heretofore no published study that systematically and

quantitatively investigates cell contact guidance characterized by biased migration in oriented collagen gels (anisotropic 3-D substratum).

It has been documented for many cell types on various isotropic substrata that cell migration can be described as a random walk with a characteristic diffusion coefficient (11), D , also termed random motility coefficient (27). Matthes and Gruler (18) proposed a mathematical description of contact guidance as a direction-dependent random walk, making an analogy to the properties of nematic liquid crystals for the case where the cell size is large with respect to the characteristic length of the structural anisotropy, which is the case for oriented collagen gel. When the structural anisotropy depends on only two orthogonal directions, which applies to an axially oriented collagen gel, the contact guidance response can then be characterized by two diffusion coefficients, $D_x (= D_{\parallel})$ and $D_y (= D_{\perp})$, in the two principal directions, x and y (where we will take the x -direction as that which defines the axial direction). They defined a polar order parameter, P_2 , to quantify the anisotropy of the diffusion (assuming $D_x > D_y$):

$$P_2(\Delta n) = \frac{D_x(\Delta n) - D_y(\Delta n)}{D_x(\Delta n) + D_y(\Delta n)} = \frac{1}{2} \frac{D_x(\Delta n) - D_y(\Delta n)}{\langle D(\Delta n) \rangle}, \quad (1)$$

where $\langle D(\Delta n) \rangle$ signifies the direction-averaged diffusion coefficient. We explicitly indicate here that all these parameters generally depend on a parameter that quantifies the contact guidance field, the birefringence, Δn , for the case of an axially oriented gel. P_2 is thus an index of axially biased migration. (See Dunn (6) for a discussion of how the general mathematical description of contact guidance depends on the specification of three principal directions, reflecting the nonuniqueness of direction in bidirectional migration, and thus has a tensor property, in contrast to the vector property of taxis where specification of one principal direction suffices.)

If $\langle D(\Delta n) \rangle$ varies significantly with Δn , then Eq. 1 may not simply reflect biased migration in the x -direction. An alternative biased cell migration index that we report here is the anisotropic diffusion parameter, $D_A(\Delta n)$:

$$D_A(\Delta n) = \frac{D_x(\Delta n)}{D_y(\Delta n)}. \quad (2)$$

Matthes and Gruler (18) cited a result of Furth (10) that generalizes the time dependence of the mean-squared total displacement, $\langle d^2(t) \rangle$, for a correlated random walk in n_d dimensions on an isotropic planar substratum in terms of the (direction-independent) diffusion coefficient, D , and directional persistence time, P (23):

$$\langle d^2(t) \rangle = 2n_d D \left\{ t - P \left[1 - \exp\left(-\frac{t}{P}\right) \right] \right\} \quad (3)$$

to the case of an axially oriented planar substratum ($n_d = 2$), assuming that P is independent of direction:

$$\langle w^2(t) \rangle = 2n_d D_w \left\{ t - P \left[1 - \exp\left(-\frac{t}{P}\right) \right] \right\}, \quad (4)$$

where the following formula relates D_w , P , and root-mean-squared cell speed, s_w , in direction w ($= x$ or y):

$$D_w = \frac{s_w^2 P}{n_d}. \quad (5)$$

Note that $n_d = 1$ in Eqs. 4 and 5 since the components of total displacement are being described (*i.e.*, $w(t) = x(t)$ or $y(t)$) although Eqs. 4 and 5 still apply with $n_d = 2$ for $w(t) = d(t)$.

They observed the contact guidance response of PMN on three planar substrata with different degrees of structural anisotropy (optical grid, with parallel lines of deposited chromium at 5 μm separation; aluminum plate, with machined parallel grooves at $11 \pm 3 \mu\text{m}$ separation and 3 μm depth, axially stretched polyethylene foil, exhibiting birefringence and characterized with an orientation parameter defined analogously to Eq. 6 of 0.3). Surprisingly, the cell orientation distributions were bimodal in each case, with orientation being biased in the y -direction almost as much as the x -direction (Fig. 4a in 18). Further, by direct estimation of $\langle s^2(\theta) \rangle$ from short-time incremental displacements, they found that the ratio $2D(\theta)/\langle s^2(\theta) \rangle$ ($= P$ from Eq. 4) was not independent of θ , the angle with respect to the x -direction, in the case of the stretched polyethylene foil. Thus, the assumption underlying Eqs. 4 and 5 that P is direction-independent is not necessarily valid. Defining a cell orientation polar order parameter, $P_{2\text{or}}$:

$$P_{2\text{or}} = 2 \langle \cos^2 \theta_c \rangle - 1 = \langle \cos^2 2\theta_c \rangle, \quad (6)$$

where θ_c is the cell orientation with respect to the x -direction, they found that $P_{2\text{or}} \ll P_2$ in all cases ($P_{2\text{or}} \approx P_2$ when they neglected orientation in the y -direction). We have defined $O_c \equiv P_{2\text{or}}$ in Guido and Tranquillo (12), and in this study we use $O_c(\Delta n)$ for a biased cell orientation index along with our definition of $D_A(\Delta n)$ for a biased cell migration index.

Noble (20) described a computer-assisted optical sectioning system to study 3-D cell migration in collagen gel. The coordinates of each cell were determined using a 3-D converging squares algorithm in a cubic electronic tracking window around each cell (any 3-D cell tracking algorithm based on light microscopic images is necessarily computationally intensive because of the difficulties presented by out-of-focus cells). It was shown that fibroblasts in collagen gel tended to move bidirectionally (22), although not with preference for any direction based on statistical analysis of displacement vectors (21). The possible formation of oriented fibrils during fibrillogenesis because of surface interactions must be considered when

interpreting data of cell migration in collagen gel. For example, strongly birefringent regions were observed near the wall of Petri dishes, whereas the gel in areas distant from the edges appeared to be essentially isotropic (19). Thus, the regions of the collagen gels used by Noble and coworkers were evidently isotropic.

Parkhurst and Saltzman (24) reported cell tracking results for PMN in collagen gels that were also evidently isotropic based on the agreement observed with Eq. 3. The measured tracks were 2-D projections of the actual 3-D tracks exhibited by cells in the volume of gel corresponding to the depth of field of the 20 \times objective. In order to track sufficient cells to obtain satisfactory precision of parameter estimates (determined to be 100 by analysis of numerically simulated cell tracks), it was necessary to pool results from six separate experiments since only 10 to 20 cells were typically in the field of view. Although necessary given the limitations of their tracking system, this is undesirable given the likely variation of collagen gel and PMN properties between preparations.

In this study, we continue and extend the computer-assisted cell tracking in collagen gels by Noble and coworkers, the diffusion characterization of random cell migration in isotropic collagen gels by Parkhurst and Saltzman, and the anisotropic diffusion characterization of contact guidance on anisotropic planar substrata by Matthes and Gruler in characterizing fibroblast contact guidance in oriented collagen gels. We describe our computer-assisted cell tracking methods in detail as well as present the data generated by using our methods, both being novel to our knowledge. Specifically, we describe three types of computer-assisted tracking methods appropriate for blood and tissue cells migrating in 3-D collagen (or fibrin) gel and present results for each.

One method tracks a relatively small number of cells in 3-D, individually at high magnification (one cell per field of view); another tracks multiple cells in a field of view in 3-D, simultaneously at low magnification but with limited depth resolution (via coarse optical sectioning) and requiring a cell matching algorithm between time points to reconstruct tracks; the third is a similar low magnification method that only generates projected 3-D tracks (no depth determination), allowing many more fields of view to be monitored simultaneously in time lapse and thus more cells to be tracked per time-lapse interval. We analyze the cell tracks obtained for human foreskin fibroblasts exhibiting contact guidance in oriented collagen gels as an anisotropic diffusion, and thereby extend our previously reported (12) contact guidance correlation between collagen fibril orientation and biased cell orientation to biased cell migration. We do so for a more extended range of gel birefringence than previously reported, obtained by using a higher strength magnetic field (5 T) and wider range of fibrillogenesis temperatures (30–40°C). Thus, we present

here correlations of axially biased ($D_A(\Delta n)$) and direction-averaged ($\langle D(\Delta n) \rangle$) cell migration with axial fibril orientation (quantified by gel birefringence, Δn), and of biased cell migration with cell orientation $O_c(\Delta n)$.

MATERIALS AND METHODS

The cell cultures, guidance chambers, and automated microscopy/image analysis workstation have been previously described (12). Essential details are given below.

Cell Cultures

Human foreskin fibroblasts (HFF) were obtained using a primary explant technique (9) and kept in liquid nitrogen after slow freezing. A cell line was initiated for culture by thawing the contents of a vial and centrifuging at 1,000 rpm for 10 min at room temperature. The resulting pellet was resuspended in fresh Dulbecco's modified Eagle's medium (DMEM) supplemented with fungizone, penicillin-streptomycin, and L-glutamine. Cells were plated out in 75 cm² culture flasks using 12 ml of DMEM with 20% fetal bovine serum (FBS) and kept in a humidified 10% CO₂ incubator at 37°C. At confluency, cells were passed using trypsin and plated out 1:4 in flasks. Cells were discarded after the 15th passage and a new cell line was initiated.

Collagen Gels

Collagen gels were prepared with the following composition (volume basis): HEPES (2%), 0.1 M NaOH (13.2%), 10 \times minimum essential medium (MEM) (10%), FBS (6.7%), penicillin-streptomycin (0.1%), L-glutamine (1%), and Vitrogen 100 (Celtrix Laboratories, Santa Clara, CA) collagen solution (67%). The components and the final mixture were kept on ice to avoid gelation before exposure to the magnetic field.

Contact Guidance Chambers

The chambers used in this study consisted of a U-shaped glass plate of nominal thickness 3 mm sealed between two microscope slides glued to the glass by silicone adhesive (Fig. 1). The rectangular space so formed had a width of 1 cm, length of 4 cm, and thickness of 3 mm. In order to minimize drying and ensure sterility, a Teflon cap was placed at the open end of the chamber after filling, and a strip of Parafilm was wrapped around the cap.

Experimental Procedure

Cells suspended in DMEM with 20% FBS were added to the cold collagen solution in such a way that the initial cell concentration was 10⁴ cells/ml (the cell suspension was concentrated so as to cause negligible dilution of the collagen solution). A low cell concentration was desired in order to minimize cell traction-induced restructuring of the fibril orientation imposed by the magnetic field and

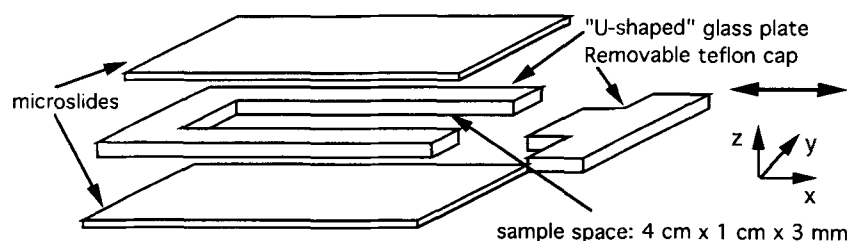


FIGURE 1. Contact guidance observation chamber. Double arrow indicates long axis of chamber, designated the *x*-direction, which is the axis of magnetically induced collagen fibril orientation. Not drawn to scale.

changes in the medium composition (it was not possible to change the medium in the chambers).

The chambers, previously sterilized in an autoclave, were loaded, capped, and sealed with Parafilm and kept on ice before being exposed to the magnetic field. Because the superconducting magnet used was not equipped with a system for temperature control, the chambers were placed in polystyrene insulating boxes containing water warmed to a temperature in the range 30–40°C (see below) in which the chambers were submersed. Measurements performed outside the magnets revealed that the temperature inside the boxes dropped about 1.5°C in 1 hr. The chambers were oriented with their long axis perpendicular to the direction of the magnetic field to induce orientation of the collagen fibrils along the same axis, *i.e.*, the long axis was perpendicular to the bore of the magnet (26). In order to minimize cell settling effects, chambers were inverted immediately before a 2 hr exposure to the magnetic field. Independent tests revealed that the majority of fibrillogenesis occurs well within this time at 30–40°C. Only minor cell redistribution due to sedimentation was observed at the lowest temperatures.

After removal from the magnet, the chambers were placed on the microscope stage and maintained at 37°C

with an air stream incubator. Birefringence measurements were performed prior to or during the initial cell spreading period (6–12 hr following gellation). The cell tracking program was started when a steady level of cell spreading was observed. Following the tracking period, birefringence measurements were again performed.

Automated Microscope/Image Analysis Workstation

The inverted microscope used in this study was a Zeiss Axiovert 10 (Zeiss, Thornwood, NY) equipped with a halogen lamp for transmitted light. All cell tracking was performed in brightfield using a long working distance (LD) condenser (70 mm) with numerical aperture (NA) = 0.3, a 10×/0.3 NA Plan-Neofluar objective (Hamamatsu, Bridgewater, NJ), a 40×/0.6 NA LD Achromplan objective (Kontron, Eching, Germany), and a 2.5× Optovar lens (Panasonic, Secaucus, NJ). Imaging was performed by sending all the light with a beam-splitting prism to a Hamamatsu CD 2400-07 Newvicon video camera system provided with independent controls of gain and offset for contrast enhancement.

The video camera was interfaced to a Kontron IBAS image processing and analysis system (386-based MIAP-2). A schematic of the system is presented in Fig. 2. The

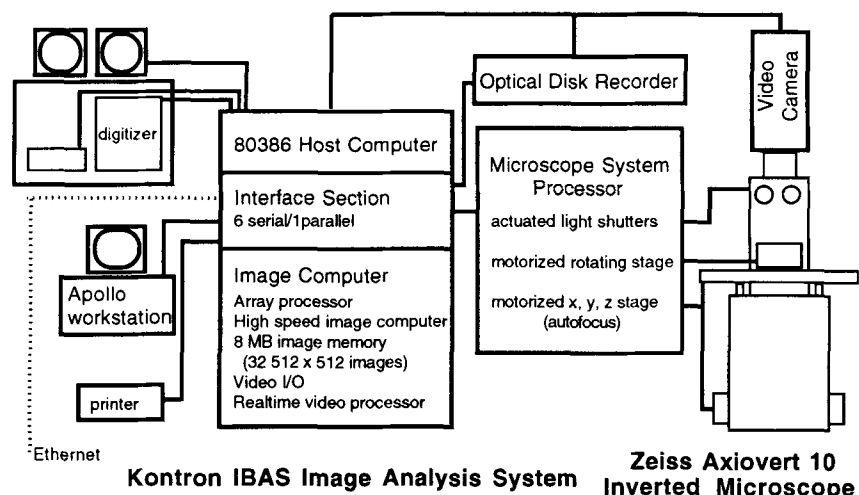


FIGURE 2. Schematic of automated microscopy/image analysis workstation.

analog signal coming from the video camera was converted by an 8-bit digitizer into an array of digital values, ranging from 0 to 255, displayed on a monitor as gray levels. The IBAS system includes a number of routines for image enhancement and image analysis that are accessible at a programming level, which we incorporated into structured macros for automatic execution. A Panasonic TQ-2028F optical disk recorder (Panasonic, Secaucus, NJ) was used to store images for subsequent verification of macro execution.

An important feature of our workstation that was exploited for cell tracking is the Zeiss 3-axis motorized translating microscope stage (Zeiss, Thornwood, NY), which enables the sample to be moved in 3-D under computer control (Zeiss MSP 65 controller). The optically encoded motors of the translating stage allow high precision movement in 0.25 μm increments in the x - and y -axes and the nose piece in 0.05 μm increments in the z -axis (<0.75 μm repeatability). Other features of the workstation that enable automated birefringence measurements are described by Guido and Tranquillo (12).

Automated Gel Birefringence Measurements

Our procedure for automated data acquisition of mean gray level *versus* sample rotation angle (with and without a compensator in the light path) and fitting governing theoretical optics formulas to these data to determine extinction angles and retardation (from which Δn is computed), is fully described in Guido and Tranquillo (12).

Automated Cell Tracking

We have developed three different methods to track cells migrating in 3-D gels (*i.e.*, within translucent collagen- and fibrin-based gels) that exploit various features of our workstation. We present each here with a discussion of their respective merits and limitations.

Single Cell 3-D Tracking at High Magnification

This method requires a magnification such that one cell fills nearly the entire IBAS measurement window (*i.e.*, the image monitor). For the HFF used in this study, we found the 40 \times objective and 2.5 \times Optovar to be appropriate (yielding a measurement window of 108 $\mu\text{m} \times 82$ μm with the camera magnification). First, the origin of the translating stage is initialized. Then, a representative cell is focused, and by imposing an offset on the video signal and amplifying with the camera gain, the contrast in the video signal is enhanced (17). An optimal gray level threshold is chosen to yield a binary image that retains the maximum cell area without including significant background, thereby discriminating the darker cell from the lighter background of the gel. A number of cells, determined by the ratio of the desired time-lapse interval to the

required image processing time per cell, are then manually selected in the collagen gel, within the volume characterized for birefringence.

When selected, a cell is focused and positioned approximately in the center of the image monitor by moving the sample with the motorized stage's trackball (with a known calibration of a motor step, this allows the present x,y,z -stage coordinates to be recorded by the computer). The gray level image is then processed to yield a binary image as follows. First, the original gray level image is processed with a high-pass filter to remove any low-frequency shading differentials. Then the resulting gray level image is made binary by using the user-initialized gray level threshold. Finally, any "holes" in the binary image of the cell are automatically filled (see the Appendix of Dickinson *et al.* (2) for an image sequence corresponding to these operations for melanoma cells in collagen gel). The cell's x,y -centroid coordinates and orientation, θ_c , are measured using standard IBAS functions (the x,y -centroid is computed from the chain code of the binary image of projected area; the measurement of θ_c is detailed below). The cell's present x,y -coordinates (relative to the stage origin) are computed by adding its measured x,y -centroid coordinates (relative to the image origin) to the present x,y -stage coordinates, and its present z -coordinate is taken to be that of the stage. ($x,y,z,\theta_c;t$) for the cell is then stored in a data array.

Once all the cells have been selected, macro execution proceeds with the computer automatically centering the stage at the first cell's initial coordinates. Its present coordinates will in general be different because of cell migration or changes in cell shape during the time elapsed since its selection (*i.e.*, the cell will appear off-center and out-of-focus). The IBAS autofocus feature is used to determine automatically the new plane of focus, that is, the present z -coordinate (autofocus determines the plane of maximum contrast change based on the greatest change in average gray value (over ten video lines) between image planes over 50 image planes sampled at 0.25 μm increments above and below the plane of focus at the last time point). The present x,y -coordinates are then determined after generating a binary image (as described above) and the stage moves to recenter the cell. The success of these operations thus hinges on the requirement that the magnification be sufficiently high so that only one cell will be present in the image. The same sequence of operations, which requires 25 sec, is automatically repeated for the second cell by the workstation, and so forth until the time-lapse interval, Δt , elapses and the loop is repeated.

Figure 3 shows a sequence of the images of the same cell migrating in an isotropic collagen gel recorded in time-lapse, following the automatic refocusing and recentering steps at each time point. In Fig. 4, the x,y,z -coordinates of the cell along with its directional orienta-

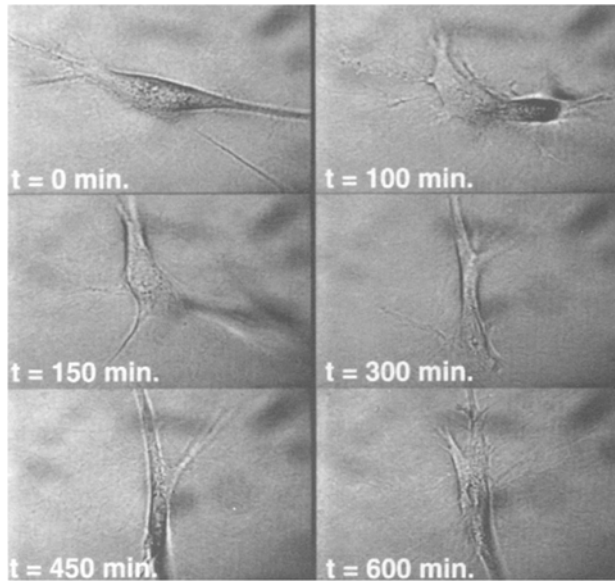


FIGURE 3. Video time-lapse sequence from Single Cell 3-D Tracking at High Magnification method showing a tracked cell centered and in-focus at selected time points. Varying cell morphology and network structure of local collagen fibrils reflects cell migration. Cell division occurs during $t = 100$ – 150 min with one daughter cell being tracked subsequently.

tion, θ_c , are plotted as a function of time clearly showing that the cell migrates a considerable distance over the 10 hr period. In order to track the maximum number of cells, Δt is chosen to be as large as possible. That is, Δt is chosen just small enough based on typical cell speeds so that a cell won't move completely outside the field and depth of view defined by its previous coordinates. Given the relatively slow speed of fibroblasts in collagen gel (reported by Heath and Hedlund (16) to be 0.3 – $0.5 \mu\text{m}/\text{min}$) this is not a severe constraint, with 30 min proving reliable for the stated imaging conditions. Thus, up to 60 cells can be tracked simultaneously with this method.

The main advantages of the Single Cell 3-D Tracking at High Magnification method are that cells can be tracked with very low probability of misidentification between time intervals, accurate assessment of migration in the z -dimension is obtained, and the potential exists for obtaining estimates of cell speed from incremental displacements as well as estimates of cell shape descriptors. The main disadvantage, alluded to previously, is the relatively small number of cells that can be tracked because of the intensive image processing required on-line for each cell at each time point (1 cell/25 sec or 2.4 cells/min). Theoretical statistical analysis of Eq. 3 reveals that the precision of parameter estimates based on tracking cells in multiple chambers simultaneously (spanning a range of Δn) is too low to be conclusive about variations of D_A with Δn (*i.e.*, large standard deviations result for $D_A(\Delta n)$).

Multiple Cell 3-D Tracking at Low Magnification

The original motivation for devising this method was to remedy the main disadvantage of the previous method. In contrast, this one tracks multiple cells in a field of view at low magnification but with limited resolution in depth (via coarse optical sectioning), requiring a cell matching algorithm between time points to reconstruct tracks. As will be seen, a larger number of cells can be tracked with this method at the cost of possible matching errors yielding inaccurately reconstructed tracks, less precision in the z -coordinate measurement (hence small displacement-based speed measurements), and less precision in cell shape descriptors. However, if the objective is to estimate only direction-dependent cell diffusion coefficients, as in this study, the latter two costs are irrelevant and this method is potentially superior (depending on the tradeoff between the increase in the number of cells tracked and the decrease in accuracy of reconstructed tracks).

An IBAS macro was written to measure and store the x, y -coordinates of multiple cells in the field of view and then to measure their approximate z -coordinates within the gel. A predefined volume within the gel is prescribed to be scanned automatically for imaging cells using the $10\times$ objective. As before, this volume is chosen to be contained within the volume for which birefringence measurements are made. The automatic scanning is accomplished by defining a 2-D x - y meander across a plane in the upper portion of the gel, involving a series of adjacent fields ($1,160 \mu\text{m} \times 870 \mu\text{m}$). For each x - y field, the gel beneath is optically sectioned digitally by acquiring and operating on images for a series of prescribed z -sections. The purpose in the first of two sequential loops (Fig. 5) is to generate a measurement window for each cell, defined by its in-focus projected area (which is needed for loop II), and not to measure its z -coordinate (which is performed in loop II); therefore, a relatively large z -increment, Δz , is used for efficiency. We found that $\Delta z > 100 \mu\text{m}$ can result in poor definition of the measurement window for some cells and therefore used $\Delta z = 50 \mu\text{m}$ in this study.

A deblurring algorithm based on using a high-pass filter to remove "out-of-focus information" (2) is used to develop a composite image of the projected cell images for all cells in the thickness of gel optically sectioned as follows (Fig. 6). A high-pass filter is applied to the first gray level (live) image to remove most of the low spatial frequency (blurred or out-of-focus) information yielding the top optical section. The minimum gray values (black = 0) comparing this filtered image to the composite image (initialized to be white) are then saved in the composite image on a pixel-by-pixel basis. This sequence is repeated for each additional z -section for the present x - y field. The

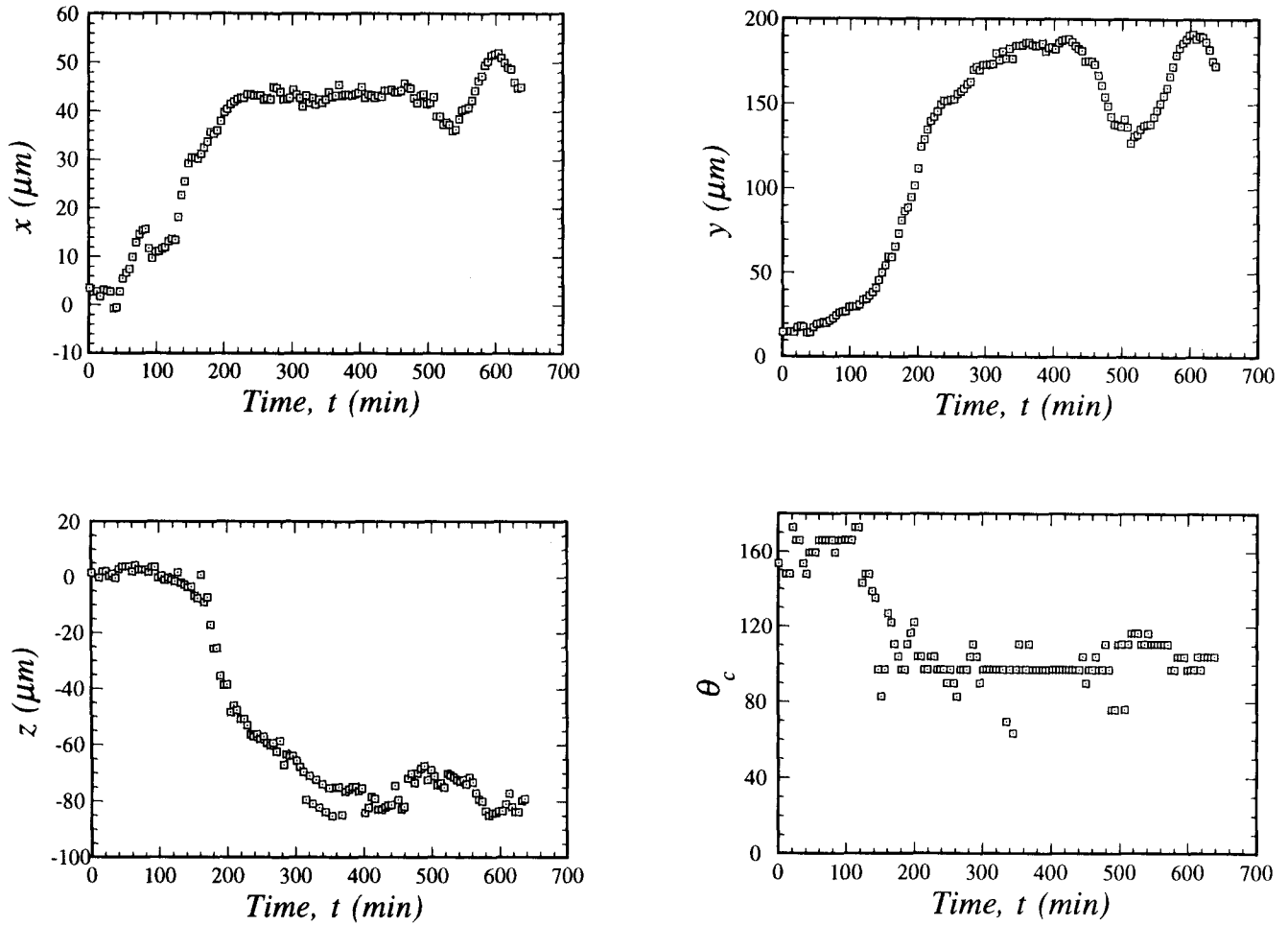


FIGURE 4. The x, y, z -coordinates, which are used to compute $\langle x^2(t) \rangle$, $\langle y^2(t) \rangle$ and $\langle z^2(t) \rangle$, and cell orientation (θ_c) which is used to compute O_c for the cell tracked in Fig. 3.

result is that the final composite contains a reasonable rendering of an in-focus image for each cell in the volume of gel thus optically sectioned. A binary image is then obtained from the composite gray level image by employing two image processing steps in addition to those already described for the Single Cell 3-D Tracking at High Magnification method: following the filling of any "holes" in the binary images of the cells, any overlapping cells are separated with an erosion-dilation cycle. Finally, any remaining binary objects that do not correspond to an area of reasonable value for a cell ($320\text{--}3,200 \mu\text{m}^2$) are removed. Standard IBAS functions are then used to measure the x, y -centroid coordinates for each cell and create a measurement window defined by its measured (projected) area.

Loop II then begins by moving the translating stage back to the top focal plane. The IBAS measurement window is defined to be the set of cell measurement windows. Since the purpose of loop II is to estimate each cell's

z -coordinate, a smaller Δz than in loop I is used. Beginning at the top and at each successive z -section, the mean gray level in each cell's measurement window is measured. A cell's z -coordinate is defined to be that where the mean gray level in the window exhibits the largest incremental change (equivalent to a rapid change in contrast when going from in-focus to out-of-focus). A tradeoff obviously exists between precision of the z -coordinate ($\approx \Delta z$) and execution time ($\propto \Delta z^{-1}$, the number of z -steps). Given a prescribed tracking period and *a priori* estimate for D_z , the z -increment required to measure D_z with a target precision can be estimated, in principle, with the methods summarized in the Data Analysis section below. We found empirically that $\Delta z = 25 \mu\text{m}$ gave acceptable results given the conditions and 12–24 hr tracking periods used in this study.

The x – y meander continues with both loops being executed at each x – y field until Δt elapses, at which time the translating stage recenters the top focal plane of the first

```

Define volume for tracking cells
While (time < total tracking period)
  Move to first x-y field
  While (time < time lapse interval)
    Move to top of next x-y field
    Set composite image white
    While (not at bottom of current x-y field)      'Loop I
      Obtain live image
      Create high-pass filter image
      Update composite image with
        min (filtered image, composite image)
      Step  $\Delta z = 50 \mu\text{m}$ 
    Repeat
    Create binary image of composite image and enhance
    Measure x,y-centroids of objects (cells) and compute x,y-coordinates
    from present stage position
    If (Multiple Cell 3-D Tracking at Low Magnification)      'Loop II
      Move to top of current x-y field
      Define measurement window for each
        object (cell) in binary image from Loop I
      While (not at bottom of current x-y field)
        Obtain live image
        For (all measurement windows)
          If (change in gray value > maximum so far)
            Assign stage z-position as object (cell) z-coordinate
          Step  $\Delta z = 25 \mu\text{m}$ 
        Repeat
      Repeat
    Repeat
  Repeat
Apply cell matching algorithm

```

FIGURE 5. Pseudocode for Multiple Cell 3-D Tracking at Low Magnification (loops I and II) and Multiple Cell Projected 3-D Tracking at Low Magnification (loop I only).

x - y field and repeats the meander. In this fashion, a data array of cell x,y,z -coordinates for each x - y field at each time point is generated. After the total tracking period has elapsed, the resulting time sequence of data arrays are transferred to an Apollo workstation. A FORTRAN program reconstructs cell tracks using an algorithm that attempts to match the elements of the arrays of cell coordinates between time points for each x - y field. The details for the case where the cell positions are represented by only the x,y -coordinates, as generated by the method presented next (Multiple Cell Projected 3-D Tracking at Low Magnification), are described elsewhere (2). Briefly, it matches as many cells as possible at one time point with the nearest neighbor cells at the next time point based on the displacement being less than some maximum, d_{max} , related to the estimate of maximum cell speed. Taking that to be $1 \mu\text{m}/\text{min}$ (twice that reported by Heath and Hedlund (16)), then for our standard 45 min time-lapse, $d_{\text{max}} \approx 45 \mu\text{m}$. For the matching algorithm to be successful, the mean separation distance between cells, d_{sep} , should be many times d_{max} . For a cell concentration of 10^4 cells/ml, $d_{\text{sep}} \approx 450 \mu\text{m}$ for 3-D and 225 for projected 3-D (based on cubic and square lattices, respectively). In this study,

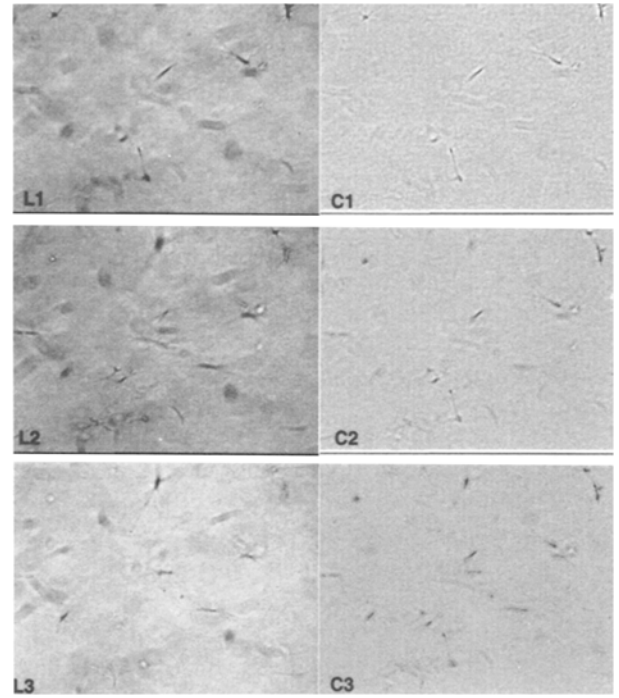


FIGURE 6. "Coarse optical sectioning" digital image processing for creation of a composite image using a deblurring algorithm based on high band-pass filtering (see text for details). A sequence of three live gray images (L1–L3) and the corresponding cumulative composite images (C1–C3) are shown. Cells appearing in-focus in L1 or L3, but not in both, are rendered reasonably in-focus in C3.

we use $d_{\text{max}} = 50 \mu\text{m}$ for matching in reconstruction of projected 3-D tracks and $d_{\text{max}} = \sqrt{3/2} \cdot 50 \mu\text{m} = 61.2 \mu\text{m}$ for full 3-D tracks (the factor $\sqrt{3/2}$ accounts for three versus two dimensions (24)).

A complication arises when the cell positions are represented by x,y,z -coordinates as obtained in this matching algorithm because of the inherently lower precision in the z -coordinate associated with a prescribed z -increment in the stage position, Δz , in contrast to only the positioning error in the x,y -coordinates (e.g., stage movement error, fluctuating cell morphology, imperfect cell outline definition, etc.). We account for this by adjusting the d_{max} criterion with a weighting factor, w_z , for cell displacement in the z -direction during Δt :

$$\Delta x^2 + \Delta y^2 + w_z \Delta z^2 < d_{\text{max}}^2. \quad (7)$$

We expect that w_z should be approximately the ratio of the mean-squared x,y -positioning error to the square of the prescribed z -increment. The choice of w_z is further described in the Results section.

Under our standard conditions (i.e., cell concentration of 10^4 cells/ml, $10\times$ magnification, $\Delta z = 50 \mu\text{m}$ in loop I and $25 \mu\text{m}$ in loop II), this method tracks ≈ 200 cells with a 45 min time-lapse interval (including a 7.5 min

contingency time buffer), or ≈ 5.3 cells/min, a tracking rate 2.2 times greater than the Single Cell 3-D Tracking at High Magnification method. This is a significant enhancement with a resultant increase in estimated parameter precision from the regression analysis because of the larger number of cells tracked.

Multiple Cell Projected 3-D Tracking at Low Magnification

The tracking rate can be increased to at least six times greater than the High Magnification method if determination of the cell z -coordinate is unnecessary. This is the case for characterizing contact guidance in our axially oriented gels with D_A since only x, y -coordinates are needed to estimate D_x and D_y . The increase occurs because loop II in the Multiple Cell 3-D Tracking at Low Magnification method need not be executed. In this case, then, cell tracking is based on the projection of the 3-D cell track into the x - y plane. In fact, the image processing steps of loop I can be performed off-line on the image sequence recorded in time-lapse so that only image acquisition and storage needs to be performed, resulting in a very large increase in the tracking rate. However, we performed loop I on-line in this study, tracking ≈ 600 cells with a 45 min time-lapse interval (tracking rate of 16 cells/min) in four different samples, or ≈ 150 cells/sample.

Data Analysis

To quantify the cell orientation distribution, the orientation parameter defined in Eq. 6 was used, which we will refer to as O_c consistent with our previous work (12). O_c varies between 0–1 as the cell orientation with respect to the axis of fibril orientation, θ_c , varies from random to perfect. θ_c was measured as the orientation of a cell's maximum Feret diameter (32 directions separated by 5.6° increments being sampled) with respect to the long axis of the chamber (x -axis), which corresponds to the axis of fibril orientation. We have previously shown this measurement to be quite accurate because the cells are typically elongated in the gel (12). We also define an anisotropic orientation parameter, $O_A = \langle \cos^2 \theta_c \rangle / \langle \sin^2 \theta_c \rangle = (1 + O_c) / (1 - O_c)$ which varies between 1– ∞ as the cell orientation varies from random to perfect (note this is the same range as for D_A).

The details of the treatment of $\langle d^2(t) \rangle$ data for deducing optimal estimates of the cell diffusion coefficient, D , and directional persistence time, P , in Eq. 3 are described elsewhere (3). Briefly, $\langle d^2(t) \rangle$ was computed by averaging squared displacements for (overlapping) time intervals, t , comprising each cell track, over all cell tracks, where t took on all possible multiples of Δt . The portion of any cell track greater than 10 time-lapse intervals in total length (450 min) was considered an independent track to ensure that tracks from several cells contribute to the long-

est time point so as not to weight data preferentially for "slow" cells that are not "lost" in the matching process as frequently as "fast" cells (*e.g.*, migrate out of the field or depth of view or exceed d_{\max} during Δt). A generalized nonlinear regression based on the full theoretical variance-covariance matrix that accounts for nonidentically distributed and nonindependent residuals was then performed on Eq. 3 augmented with the mean-squared positioning error, γ (3)

$$\langle d^2(t) \rangle = 2n_d D \left\{ t - P \left[1 - \exp\left(-\frac{t}{P}\right) \right] \right\} + 2\gamma. \quad (8)$$

We applied the same approach to $\langle w^2(t) \rangle$ data using a generalization of Eq. 4 that allows for direction-dependent P :

$$\langle w^2(t) \rangle = 2n_d D_w \left\{ t - P_w \left[1 - \exp\left(-\frac{t}{P_w}\right) \right] \right\} + 2\gamma_w. \quad (9)$$

Convergence using Eq. 9 for a full three parameter fit (D_w , P_w , γ_w) was sometimes not obtained (presumably because P_w was $< \Delta t$ and γ_w was $> D_w t$ in those samples). In order to circumvent this problem, a two parameter fit (D_w , P_w) using an *a priori* estimate of γ_w was used, with $\gamma_w = 20 \pm 10 \mu\text{m}^2$ based on results from successful three parameter fits. When convergence still was not obtained, the linear long-time approximation ($t > P_w$) of Eq. 9 was used for the two parameter fit (D_w , η_w):

$$\langle w^2(t) \rangle \approx 2\eta_w D_w t + \eta_w, \quad (10)$$

where η_w is a combined parameter

$$\eta_w = 2(\gamma_w - n_d D_w P_w). \quad (11)$$

Since D_w was the only parameter we needed to estimate in this study given our goal of determining $D_A(\Delta n)$, these cases were not problematic. Note that $n_d = 1$ for x, y, z -component displacements and $n_d = 2, 3$ for total displacements for projected and full 3-D cell tracks, respectively.

RESULTS

Results from four separate experiments are reported here. One involved only one sample and is reported in the next section, Single Cell 3-D Tracking at High Magnification. The other three each involved three or four samples (spanning a range of gel birefringence) and were analyzed using the Multiple Cell Projected 3-D Tracking at Low Magnification method. Results from these three experiments are reported together in the following section. In one of these experiments, tracking data were first obtained with the Multiple Cell Projected 3-D Tracking at Low Magnification method and then, immediately follow-

ing, with the Multiple Cell 3-D Tracking at Low Magnification method (same Δt). Results using the latter method in this experiment are reported in the final section. Since the gel birefringence, Δn , did not significantly change over the tracking period when checked, in agreement with our previous finding (12), we present results in terms of Δn measured prior to the tracking period (the average of five points defining the vertices and center of a rectangular volume of gel centered in the chamber and the standard deviation are reported).

Cell Orientation

In Fig. 7 we present a summary plot of the cell orientation parameter, O_c , versus Δn for the three experiments with multiple samples (11 total). These results are in agreement with our previously reported correlation (12) and extend it to both higher and lower values of Δn .

Single Cell 3-D Tracking at High Magnification

In Fig. 8 we present $\langle x^2(t) \rangle$, $\langle y^2(t) \rangle$, and $\langle z^2(t) \rangle$ obtained from the tracks of 45 HFF tracked for 7 hr in a collagen gel that was exposed to a magnetic field of 4 T at 35°C during fibrillogenesis ($\Delta n = 9 \times 10^{-6}$). Migration bias along the axis of fibril orientation (x-direction) is obvious when comparing $\langle x^2(t) \rangle$ and $\langle y^2(t) \rangle$. Note that in each case the slope appears relatively constant over a broad intermediate time range, indicating that a diffusion description in each direction is legitimate. The curvilinearity at short times reflects directional persistence and at long times is due to the correlation between time-points being more pronounced as the sample size decreases (3). We obtain the following estimates from the generalized regression analysis: $D_x = 1.47 \pm 0.31 \mu\text{m}^2/\text{min}$, $D_y = 0.22 \pm 0.08 \mu\text{m}^2/\text{min}$, and $D_z = 1.68 \pm 0.72 \mu\text{m}^2/\text{min}$, and therefore from Eq. 2 that $D_A = 6.68 \pm 2.70$. The related results in

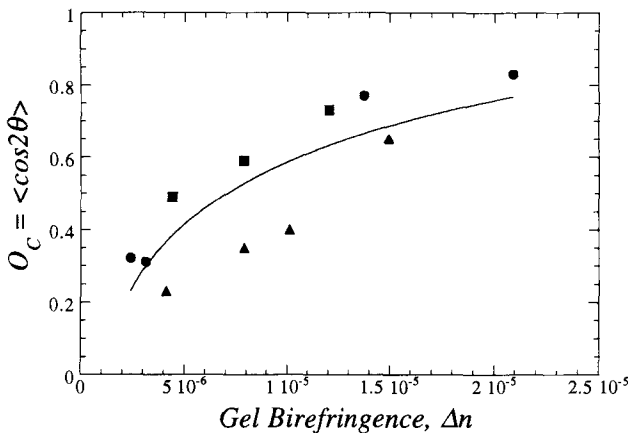


FIGURE 7. Correlation of cell orientation, O_c , with gel birefringence, Δn . Different symbols signify results from multiple samples in three different experiments.

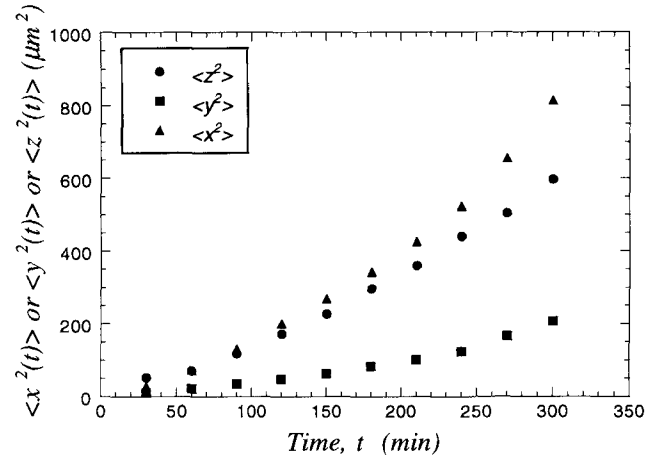


FIGURE 8. Plot of component mean-squared displacements, $\langle x^2(t) \rangle$, $\langle y^2(t) \rangle$, $\langle z^2(t) \rangle$ for a population of 45 cells tracked for ≈ 7 hr using the Single Cell 3-D Tracking at High Magnification method.

Table 1 suggest that enhanced directional persistence and (possibly) speed in the x-direction relative to the y-direction underlies the contact guidance response signified by $D_A > 1$; however, Δt was not optimized to maximize precision of these estimates (*e.g.*, σ_P is minimized for $\Delta t \approx P_w$ as discussed in (3)), so we do not consider this a conclusion. Curiously, D_z is larger than D_y (see Discussion). The large uncertainty in D_z is related to the pronounced offset in the $\langle z^2(t) \rangle$ curve which is symptomatic of positioning error (3), in this case due to the inherent imprecision in measuring the z-coordinate using the IBAS autofocus function (notice the regression estimate of the associated uncertainty $\sqrt{\gamma_z} \approx 5 \mu\text{m}$ is reasonable given that autofocus is operating on a cell that may extend 50–100 μm in the z-direction). Because our main interest is in how D_A varies with Δn , which does not require D_z (*i.e.*, the z-coordinate of the cell track), effort was concentrated on the methods for multiple cell tracking at low magnification, since their higher tracking rates allowed simultaneous tracking of cells in four samples spanning a range of Δn , with a gain in the precision in the estimate of D_A .

Multiple Cell Projected 3-D Tracking at Low Magnification

Figure 9 presents a plot of $\langle x^2(t) \rangle$ and $\langle y^2(t) \rangle$ based on reconstructed cell tracks generated by this method for one sample ($\Delta n = 1 \times 10^{-5}$). Representative recon-

TABLE 1. GLSR results for Single Cell 3-D Tracking at High Magnification.

	D_w ($\mu\text{m}^2/\text{min}$)	P_w (min)	S_w ($\mu\text{m}/\text{min}$)	γ_w (μm^2)
x	1.47 ± 0.31	65.1 ± 19.2	0.150 ± 0.015	4.90 ± 1.90
y	0.22 ± 0.08	15.6 ± 24.9	0.118 ± 0.153	1.43 ± 2.38
z	1.68 ± 0.72	151 ± 89	0.106 ± 0.021	21.1 ± 7.70

structed tracks are shown in Fig. 10. The solid lines in Fig. 9 are the fitted regression curves of the correlated random walk model (Eq. 9) and the dashed lines define the regression curves \pm the theoretical root-mean-squared residual. Note that the regression curve does not straddle the data as would be the case in an ordinary regression analysis because the generalized analysis accounts for the longer time data being increasingly correlated in time with larger variance in the residuals (3). As expected, the deviation of the data from the regression curve, although strongly correlated, is of the order of the theoretical root-mean-squared residual. The reconstructed cell tracks appear reasonable and clearly show a contact guidance response in the x -direction. Relevant descriptors for the tracking results are presented next based on the following definitions: $\langle x(t) \rangle$ and $\langle y(t) \rangle$ computed from the endpoint of all tracks of T_{\max} duration referred to a common origin ($T_{\max} = 10\Delta t = 450$ min), which theoretically should be zero if migration obeys a diffusion (*i.e.*, unbiased) in the x - and y -directions; $\langle x(t) \rangle / x_{\text{rms}}$ and $\langle y(t) \rangle / y_{\text{rms}}$ where x_{rms} and y_{rms} are the root-mean-squared displacements in the x - and y -directions over T_{\max} based on Eq. 10, which gives a measure of the significance of $\langle x(t) \rangle$ and $\langle y(t) \rangle$ being nonzero; $\langle T \rangle$, the mean track duration (over all tracks); and $\langle T \rangle / T_{\max}$, which gives a measure of the ability of the method to track a cell during the entire tracking period (reflecting the method's performance). The averages over all 11 samples are as follows: $\langle x(t) \rangle / x_{\text{rms}} = 0.081 \pm 0.200$; $\langle y(t) \rangle / y_{\text{rms}} = 0.019 \pm 0.212$; $\langle T \rangle / T_{\max} = 0.65 \pm 0.15$. From these results we conclude that our results are

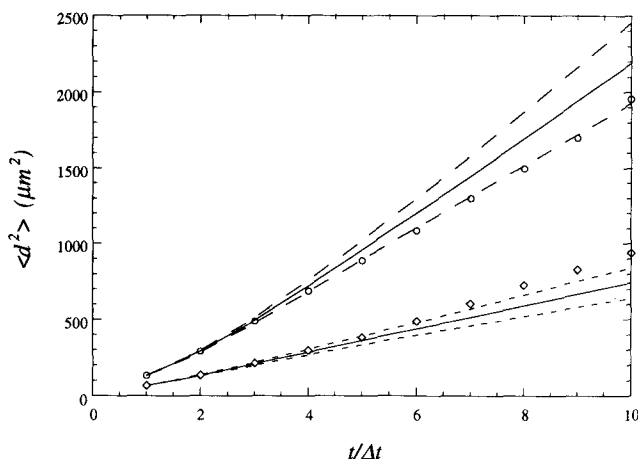


FIGURE 9. Plot of component mean-squared displacements, $\langle x^2(t) \rangle$ (circles) and $\langle y^2(t) \rangle$ (diamonds) for a population of approximately 150 cells tracked simultaneously in different x - y fields (image composites of at least five optical sections) using the Multiple Cell Projected 3-D Tracking at Low Magnification method. The solid lines are the best fits of the correlated random walk model Eq. 9 and the dashed lines define the best fit values \pm the theoretical root-mean-squared residual.

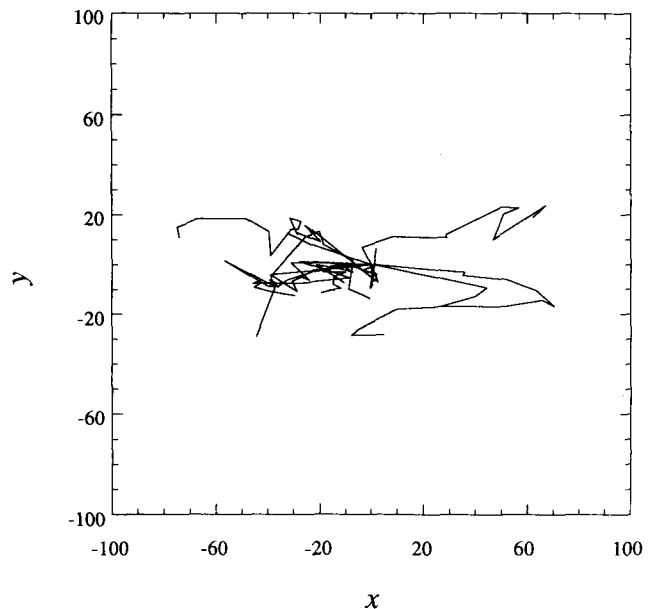


FIGURE 10. Plot of reconstructed cell tracks from one x - y field for the sample used in Fig. 9. Twelve representative tracks translated to begin at the same origin are shown. Units are in μm .

consistent with migration that is unbiased in both the x - and y -directions and with the method's ability to track cells for considerable periods via the matching algorithm.

The key results of this study are presented in Figs. 11–13: the dependencies of D_x and D_y (Fig. 11), $\langle D \rangle$ (Fig.

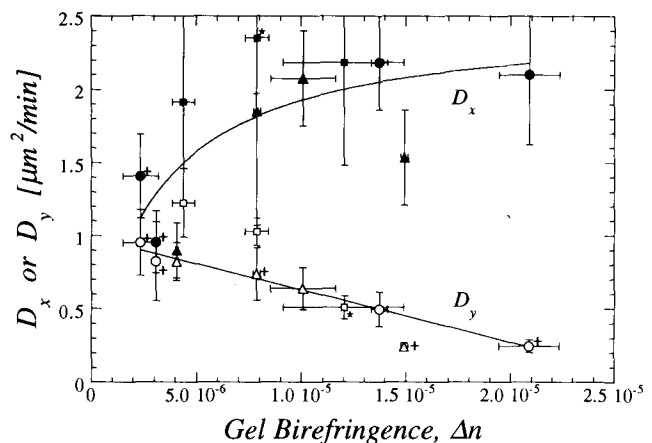


FIGURE 11. Dependence of the direction-dependent cell diffusion coefficients, D_x and D_y , on gel birefringence, Δn , based on the Multiple Cell Projected 3-D Tracking at Low Magnification method. Different symbols signify three separate experiments as in Fig. 7. Error bars for Δn are based on the sample standard deviation ($n = 5$) and for D_x and D_y are based on the standard errors of the parameter estimates from the generalized nonlinear regression fit of Eq. 9 or 10 to the $\langle x^2(t) \rangle$ and $\langle y^2(t) \rangle$ data as in Fig. 9. * and + denote cases that required two parameter fits, (D_w , P_w) and (D_w , η_w), respectively, for convergence in the generalized regression analysis (see Data Analysis).

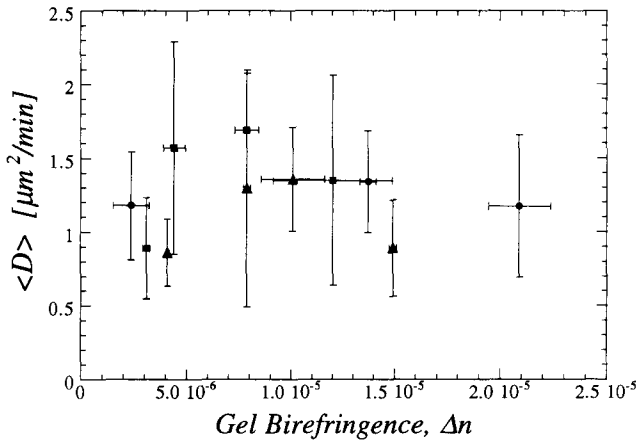


FIGURE 12. Dependence of the direction-averaged cell diffusion coefficient, $\langle D \rangle$, on gel birefringence, Δn . $\langle D \rangle = (D_x + D_y)/2$ is determined from D_x and D_y in Fig. 11.

12), and D_A (Fig. 13) on Δn over the same range as presented for O_C in Fig. 7. It can be seen that D_A increases with increasing Δn over this range (Fig. 13) and, interestingly, this is due mainly to an enhancement of migration along the axis of fibril orientation at low levels of fibril orientation (D_x rapidly increasing at small Δn), and to a suppression of migration normal to the axis of fibril orientation at high levels of fibril orientation (D_y steadily decreasing at large Δn) (Fig. 11). Also interestingly, all values of D_A are reasonably clustered around the regression curve, while such is not the case for D_x and D_y , implying that although differences in the absolute levels of migration occur among different samples having the same Δn , the contact guidance response in terms of the ratio D_x/D_y is constant. Within the uncertainty of the results, there is little dependence of $\langle D \rangle$ on Δn (Fig. 12). The plot of D_A versus O_A , the related anisotropic orientation parameter, reveals that $D_A \approx O_A$ (Fig. 14), that is, the

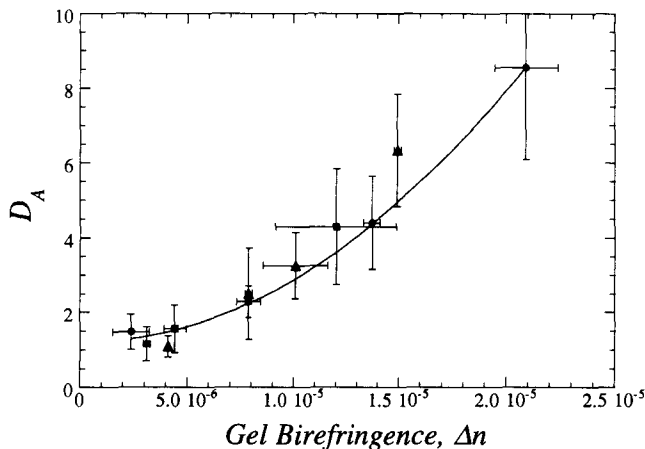


FIGURE 13. Dependence of the anisotropic cell diffusion parameter, D_A , on gel birefringence, Δn . $D_A = D_x/D_y$ is determined from D_x and D_y in Fig. 11.

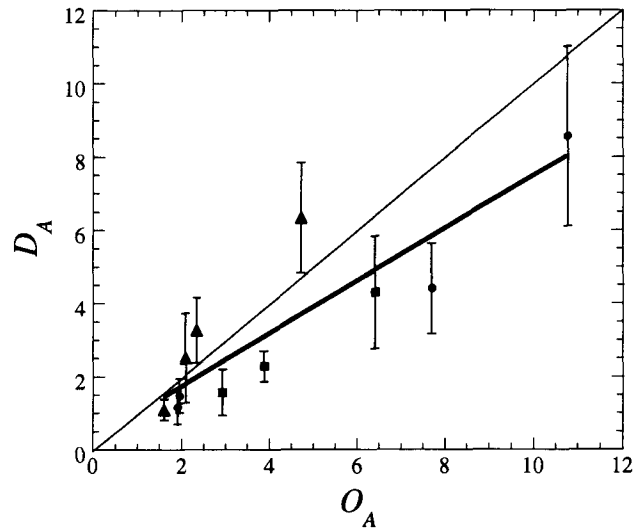


FIGURE 14. Correlation of anisotropy of cell migration (D_A) and cell orientation (O_A). D_A is from Fig. 13 and $O_A = (1 + O_C)/(1 - O_C)$ is calculated from O_C in Fig. 7. The diagonal (slope = 1) represents $D_A = O_A$. The thick line is a linear fit of the data, with slope = 0.77 ± 0.071 .

degree of anisotropy of orientation and migration are similar over the range of contact guidance elicited. Note that the values of D_x and D_y at $\Delta n = 9 \times 10^{-6}$ (Fig. 11) are in good agreement with those obtained from the Single Cell 3-D Tracking at High Magnification method.

Multiple Cell 3-D Tracking at Low Magnification

Implementation of this method requires the additional specification of the x/y to z precision ratio weighting parameter, w_z , used in the d_{\max} matching criterion (Eq. 7). We find that D_z decreases monotonically very rapidly as w_z increases from 0 to 0.01, and then very slowly as w_z increases further. This dependence can be understood in terms of supoptimal matching for nonoptimal w_z : for w_z too small, the probability that a cell will be erroneously matched with a nearest neighbor on a much different focal plane becomes high (the main concern about the Multiple Cell Projected 3-D Tracking at Low Magnification method) thus D_z becomes very large, while for w_z too large, the probability that z -displacement yields $d > d_{\max}$ becomes so high that tracks are prematurely terminated without allowing for z -displacement. Thus D_z becomes very small (consistent with our finding that $\langle T \rangle/T_{\max}$ decreases as w_z increases).

Note that $w_z \approx 0.01$ – 0.02 , which yields $D_z \approx D_x$ consistent with the results of the Single Cell 3-D Tracking at High Magnification method (Fig. 8), is approximately equal to the ratio of the estimated mean-squared x/y -positioning error ($\gamma_{x/y} \approx 20 \mu\text{m}^2$ from the regression analysis) to the squared z -increment used in loop II ($\Delta z^2 = (25 \mu\text{m})^2 = 625 \mu\text{m}^2$), our *a priori* definition for w_z based on

heuristic reasoning (this gives $w_z = \gamma_{x/y}/\gamma_z = 0.032$ for $\gamma_z = \Delta z^2$, but since there is positioning error in determination of the z -coordinate in addition to the inherent imprecision associated with Δz , this value represents an upper limit—the choice $\gamma_z = (2\Delta z)^2$, which seems a conservative estimate from our experience with the optical sectioning performance, gives a lower limit of 0.008 for w_z).

We further find that the estimated precision of D_x and D_y for $w_z = 0.01$ or 0.02 is generally lower (standard deviations are greater) for these results as compared with those for the Multiple Cell Projected 3-D Tracking at Low Magnification method. That is because significantly fewer cells are tracked per unit time ($\approx 1/3$), which is reflected in the standard deviations generated by the regression analysis. We present in Fig. 15 a plot of $D_x^{(3)}/D_x^{(2)}$ versus w_z , where $D_x^{(3)}$ is the value of D_x determined by this method for a particular w_z and $d_{\max} = 61.5 \mu\text{m}$, and $D_x^{(2)}$ is the value obtained for $w_z = 0$ and $d_{\max} = 50 \mu\text{m}$ (equivalent to the Multiple Cell Projected 3-D Tracking at Low Magnification method applied to the same set of data, *i.e.*, not utilizing the z -coordinates). The fact that $D_x^{(3)}/D_x^{(2)}$ is scattered about one for all w_z investigated in its estimated range implies that our estimation of D_x (and D_y) from projected 3-D tracks, which neglects z -displacement, does not induce a systematic bias (D_x and D_y are much less sensitive to cell mismatches in track reconstruction than D_z as w_z is varied, in accordance with our expectation). These results further support that our major results previously presented in Figs. 11–14 based on projected 3-D tracks are accurate.

DISCUSSION

We present here the first quantitative correlation for cell contact guidance in a 3-D protein network in terms of

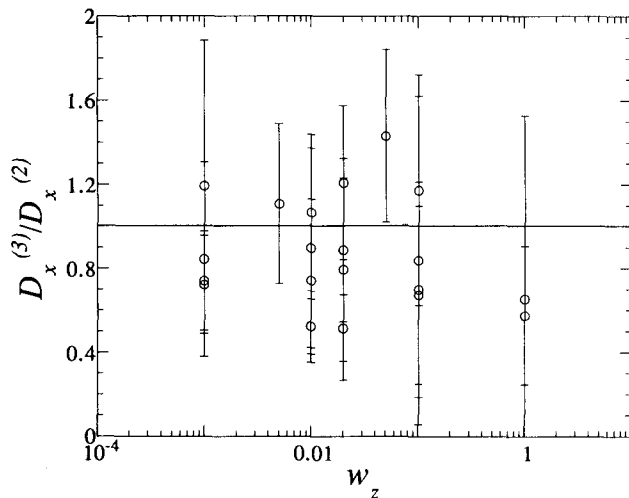


FIGURE 15. Plot of $D_x^{(3)}/D_x^{(2)}$ versus w_z to assess the accuracy of reconstructed projected paths. Note the regression analysis was not performed on all four samples at each value of w_z .

biased cell migration (Fig. 13), which relates the anisotropic cell diffusion parameter, D_A (a measure of biased cell migration), with collagen gel birefringence, Δn (a measure of collagen fibril orientation). Although correlations for contact guidance on planar substrata have been reported, mostly in terms of biased cell orientation based on static images with the exception of Matthes and Gruler (18), the unavailability of our unique combination of methodologies has heretofore precluded its study in the physiologically relevant environment of “tissue-equivalent” collagen gel. Since oriented fibrin gel can be created in a similar fashion, our methodology can be extended to study contact guidance of cells in an environment that mimics the initial state of a wound.

Our use of D_A assumes that cell migration conforms to an anisotropic diffusion, implying that mean-squared displacement in orthogonal directions varies linearly with time at sufficiently long times. Validating this is problematical in practice because of the inherent correlation between mean-squared displacement at successive time points, which causes deviation from linearity, becoming more pronounced at longer times (3). Our results appear consistent with this assumption, however, legitimizing our use of D_A , in that we can successfully fit the long-time linear form for mean-squared displacement (Eq. 10) to all data sets in the sense that the data generally fall within the theoretical root-mean-squared residual value from the regression curve.

Similarly, it is difficult to draw a conclusion from the fact that Eq. 9 cannot fit all data sets (*i.e.*, convergence is not always obtained). Possible reasons are that a direction-dependent correlated random walk model is accurate for contact guidance but there were insufficient precise short-time data in those cases, or that the model is not accurate and successful convergence only reflects a robust property of Eq. 9. It should be noted that anisotropic diffusion probably does not uniquely derive from a direction-dependent correlated random walk, that is, random walk models with other statistical properties may have long-time forms consistent with anisotropic diffusion. A rigorous mathematical theory for contact guidance that would predict the complete time dependence of mean-squared displacement, like those derived from probabilistic models of random migration (*e.g.*, 4,5,8,23), and perhaps support the accuracy of Eq. 9 has not yet been proposed.

While it is expected that the degree of anisotropy of cell orientation (O_A) and migration (D_A) are similar over the range of collagen fibril orientation (Δn) studied (Fig. 14), implying that the cell mainly migrates in the direction coincident with its polarity axis, it is perhaps unexpected that D_A increases with increasing Δn (Fig. 13) due mainly to a rapid enhancement of migration along the axis of fibril orientation at low levels of fibril orientation (small Δn), and to a continued suppression of migration normal to the

axis of fibril orientation at high levels of fibril orientation (large Δn) (Fig. 11). This trend may reflect some maximum efficiency of cell migration in the direction of highly oriented fibrils. Our study does not provide direct insight into the mechanistic basis for this phenomenon. Dunn (7) has proposed three possible mechanisms, not necessarily mutually exclusive, for contact guidance in oriented fibrillar networks: (1) focal adhesions are confined to fibrils, which since aligned (chemical anisotropy) orient the adhesions, hence locomotion; (2) the cell distorts differently when migrating in different directions, less when oriented with fibrils, due to the structural anisotropy, and hence favors locomotion oriented along fibrils; and (3), as elaborated by Haston *et al.* (15), since exertion of cell traction on the substratum is necessary for locomotion, pseudopods pulling in the direction of minimum elasticity (*i.e.*, along fibrils) are more efficient since the displacement of fibrils toward the cell is much less than for pseudopods pulling in the direction of maximum elasticity (*i.e.*, across fibrils), the result of this mechanical anisotropy again being locomotion-oriented along the fibrils.

Evaluating these alternatives in light of our correlation will require much more theoretical and experimental effort, for example mathematical models of cytomechanics relating pseudopod activity and integrin distribution with local microstructure of the surrounding collagen fibril network, and rheological and microstructural characterization of oriented collagen gel. We have evidence for a correlation of increasing cell aspect ratio (ratio of maximum to minimum Feret diameters) with increasing gel birefringence, suggesting increased cell elongation along with the increased contact guidance as collagen fibril orientation increases, which supports the relevance of (2); however, the statistical significance for this correlation, being difficult to assess (imaging was optimized for cell tracking, not cell morphology, meaning variable resolution of the projected cell outline from which the Feret diameters are derived) and therefore unknown.

Although measurement of D_A does not require D_z , nor therefore true 3-D cell tracking, we describe two very different 3-D tracking methods, Single Cell 3-D Tracking at High Magnification and Multiple Cell 3-D Tracking at Low Magnification (with respective pros and cons), that yield similar estimates for D_z (as well as D_x and D_y) for an *a priori* estimate of the weighting factor needed to apply the matching algorithm of the latter. It is not obvious why D_z is similar in magnitude to D_x instead of to D_y , although we have previously reported evidence that the fibrils are not *uniaxially* oriented (12), *i.e.*, not transversely isotropic in the y - z plane (see axes in Fig. 1)—in the uniaxial case we would expect $D_z \approx D_y$. Although fibrils appear axially oriented when viewing from above the chamber in the x - y plane (*i.e.*, biased along the long x -axis of the chamber with symmetry about the axis), our impression

when viewing from the side of the chamber in polarized light is that, across most of the thickness, fibril orientation does not appear so axially oriented. Rather, fibrils appear to be oriented diagonally quite uniformly (*e.g.*, from lower left to upper right), possibly a consequence of a recirculation pattern of the solution during fibrillogenesis. This microstructure implies contact guidance would occur in the z -direction, which would be consistent with our finding that $D_z > D_y$. It also implies that our measured values of D_x and, hence, derived values of D_A may underestimate the true values since the principal direction of the guidance field would then be along the diagonal rather than the x -axis as assumed. However, our observation of the diagonal fibril orientation was made in only the one instance we checked for uniaxial orientation when viewing from the side, which was subsequent to the experiments described herein; thus, we do not know if diagonal fibril orientation systematically occurred in these experiments.

We conclude that if information regarding migration in the depth dimension (*e.g.*, D_z) is not required, then our Multiple Cell Projected 3-D Tracking at Low Magnification method, when employed under the optimal experimental conditions (*i.e.*, yielding accurate path reconstruction), is the superior method of the three presented because of the greater number of tracked cells that contribute to the generalized least squares regression analysis of Eq. 9 and, hence, greater precision in estimates of D_x , D_y , and D_A . If such information is required, then the Single Cell 3-D Tracking at High Magnification method is presently preferred because its virtual complete accuracy in path reconstruction, in contrast to the Multiple Cell 3-D Tracking at Low Magnification method, outweighs the loss in estimated parameter precision resulting from the regression analysis because of the smaller number of cells tracked.

Our correlation of D_A with Δn provides a basis for predicting the dynamic redistribution of cells in an axially oriented fibrillar network (soft tissue or tissue-equivalent gel), even one with spatially varying orientation. This is possible using the same mathematical modeling approach by which the concentration profile of a diffusible substance is predicted given its diffusion coefficient and initial concentration distribution, albeit more complicated for the case of cell contact guidance since the diffusion is direction-dependent. This predictive capability will first require developing an empirical correlation between gel birefringence and collagen fibril orientation, as we discuss elsewhere (12). A general correlation for the case of general fibril orientation (*i.e.*, not restricted to axial orientation as obtained in our contact guidance assay chamber) is amenable to treatment with our approach, but will involve much more effort given its tensorial property. The ultimate challenge in the understanding of contact guidance in fibrillar networks is to predict *a priori* how cells will re-

distribute in response to the contact guidance field they dynamically create themselves, individually and locally via tractional structuring, and collectively and globally by deforming, thereby orienting, the fibrillar network in the course of exerting traction (resulting in time-varying fibril orientation), a potentially significant mechanism in morphogenesis and homeostasis, for example wound contraction, as suggested by the *in vitro* experiments of Harris and coworkers (13,14,25). Achieving this goal will additionally require mathematical theories relating cell traction, network deformation, and fibril orientation (1,28).

REFERENCES

1. Barocas, V.H.; Tranquillo, R.T. Biphasic model and *in vitro* assays of cell-fibril mechanical interactions in tissue-equivalent gels. In: V.C. Mow, ed. Cell mechanics and cellular engineering. Springer-Verlag: New York; 1994.
2. Dickinson, R.B.; McCarthy, J.B.; Tranquillo, R.T. Quantitative characterization of cell invasion *in vitro*: formulation and validation of a mathematical model of the collagen gel invasion assay. *Ann. Biomed. Eng.* 21:679-697; 1993.
3. Dickinson, R.B.; Tranquillo, R.T. Optimal estimation of cell movement indices from the statistical analysis of cell tracking data. *AIChE J* 39:1995-2010; 1993.
4. Dickinson, R.B.; Tranquillo, R.T. A stochastic model for adhesion-mediated cell random motility and haptotaxis. *J. Math. Biol.* 31:563-600; 1993.
5. Dunn, G.A. Characterising a kinesis response: time averaged measures of cell speed and directional persistence. *Agents Actions Suppl.* 12:14-33; 1983.
6. Dunn, G.A. Chemotaxis as a form of directed cell behaviour: some theoretical considerations. In: Lackie, J.M.; Wilkinson, P.C., eds. Biology of the chemotactic response. Cambridge University Press: Cambridge; 1981: pp. 1-26.
7. Dunn, G.A. Contact guidance of cultured tissue cells: a survey of potentially relevant properties of the substratum. In: Bellairs, R.; Curtis, A.; Dunn, G., eds. Cell behaviour. Cambridge University Press: Cambridge; 1982: pp. 247-280.
8. Dunn, G.A.; Brown, A.F. A unified approach to analysing cell motility. *J. Cell. Sci. Suppl.* 8:81-102; 1987.
9. Freshney, R.I. Culture of animal cells: a manual of basic technique, 2nd ed. Alan R. Liss, Inc.: New York; 1987.
10. Furth, V.R. Die Brownsche Bewegung bei Berücksichtigung einer Persistenz der Bewegungsrichtung. Mit Anwendungen auf die Bewegung lebender Infusorien. *Zeit. f. Phys.* II:244-256; 1920.
11. Gail, M.H.; Boone, C.W. The locomotion of mouse fibroblasts in tissue culture. *Biophys. J.* 10:980-993; 1970.
12. Guido, S.; Tranquillo, R.T. A methodology for the systematic and quantitative study of cell contact guidance in oriented collagen gels: correlation of fibroblast orientation and gel birefringence. *J. Cell. Sci.* 105:317-331; 1993.
13. Harris, A.K. Tissue culture cells on deformable substrata: biomechanical implications. *J. Biomech. Eng.* 106:19-24; 1984.
14. Harris, A.K.; Stopak, D.; Wild, P. Fibroblast traction as a mechanism for collagen morphogenesis. *Nature* 290:249-251; 1981.
15. Haston, W.S.; Shields, J.M.; Wilkinson, P.C. The orientation of fibroblasts and neutrophils on elastic substrata. *Exp. Cell. Res.* 146:117-126; 1983.
16. Heath, J.P.; Hedlund, K.-O. Locomotion and cell surface movements of fibroblasts in fibrillar collagen gels. *Scan. Electron Microsc.* 4:2031-2043; 1984.
17. Inoue, S. Video microscopy. Plenum Press: New York; 1987.
18. Matthes, T.; Gruler, H. Analysis of cell locomotion. Contact guidance of human polymorphonuclear leukocytes. *Eur. Biophys. J.* 15:343-357; 1988.
19. Modis, L. Organization of the extracellular matrix: a polarization microscopic approach. CRC Press: Boca Raton; 1991.
20. Noble, P.B. Extracellular matrix and cell migration: locomotory characteristics of MOS-11 cells within a three-dimensional hydrated collagen lattice. *J. Cell. Sci.* 87:241-248; 1987.
21. Noble, P.B.; Boyarsky, A. Analysis of cell three-dimensional locomotory vectors. *Exp. Cell. Biol.* 56:289-296; 1988.
22. Noble, P.B.; Shields, E.D. Time-based changes in fibroblast three-dimensional locomotory characteristics and phenotypes. *Exp. Cell. Biol.* 57:238-245; 1989.
23. Othmer, H. G.; Dunbar, S. R.; Alt, W. Models of dispersal in biological systems. *J. Math. Biol.* 26:263-298; 1988.
24. Parkhurst, M.R.; Saltzman, W.M. Quantification of human neutrophil motility in three-dimensional collagen gels. *Biophys. J.* 61:306-315; 1992.
25. Stopak, D.; Harris, A.K. Connective tissue morphogenesis by fibroblast traction. I. Tissue culture observations. *Dev. Biol.* 90:383-398; 1982.
26. Torbet, J.; Ronziere, M.C. Magnetic alignment of collagen during self-assembly. *Biochem. J.* 219:1057-1059; 1984.
27. Tranquillo, R.T.; Alt, W. Glossary of terms concerning oriented movement. In: Alt, W.; Hoffman, G., eds. Biological motion. Springer-Verlag: Berlin; 1990, Vol. 89: pp. 510-517.
28. Tranquillo, R.T.; Durrani, M.A.; Moon, A.G. Tissue engineering science: consequences of cell traction force. *Cytotechnology* 10:225-250; 1992.